Designing a Hybrid Electrode Towards High Energy Density with a Staged Li^+ and PF_6^- De/intercalation Mechanism

Junnan Hao [a,b], Fuhua Yang [a], Shilin Zhang [a], Hanna He [a], Guanglin Xia [a,c*], Yajie Liu [a], Christophe Didier [a,c], Tongchao Liu,[e] Wei Kong Pang [a], Vanessa K. Peterson [d], Jun Lu [e*], Zaiping Guo [a,b*]

[a] Institute for Superconducting and Electronic Materials, Australian Institute for Innovative Materials, University of Wollongong, Wollongong, NSW 2522, Australia.

[b] School of Mechanical, Materials, Mechatronic, and Biomedical Engineering, Faculty of Engineering & Information Sciences, University of Wollongong, NSW 2500, Australia.

[c] Department of Materials Science, Fudan University, Shanghai, 200433 China

[d] Australian Centre for Neutron Scattering, Australian Nuclear Science and Technology Organization, Locked Bag 2001, Kirrawee DC, NSW, 2232, Australia

[e] Chemical Sciences and Engineering Division, Argonne National Laboratory,

Lemont, IL 60439, USA

*e-mail: guanglin@uow.edu.au; junlu@anl.gov; zguo@uow.edu.au

Abstract

Existing lithium-ion battery technology is struggling to meet our increasing requirements for high energy density, long lifetime, and low-cost energy storage. Here, a hybrid electrode design is developed by a straightforward re-engineering of commercial electrode materials, which has revolutionized the "rocking chair" mechanism by unlocking the role of anions in the electrolyte. Our proof-of-concept hybrid $LiFePO_4$ (LFP)/graphite electrode works with a staged de/intercalation mechanism of Li^+ cations and PF_6^- anions in a broadened voltage

range, which was thoroughly studied by *ex-situ* X-ray diffraction, *ex-situ* Raman spectroscopy, and *operando* neutron powder diffraction. Introducing graphite into the hybrid electrode accelerates its conductivity, facilitating the rapid extraction/insertion of Li^+ from/into LFP phase in 2.5-4.0 V. This charge/discharge process, in turns, triggers the *in-situ* formation of the cathode/electrolyte interphase (CEI) layer, reinforcing the structural integrity of the whole electrode at high voltage. Consequently, this hybrid LFP/graphite-20% electrode displays a high capacity and long-term cycling stability over 3500 cycles at 10 C, superior to LFP and graphite cathodes. Importantly, the broadened voltage range and high capacity of the hybrid electrode enhance its energy density, which is leveraged further in a full-cell configuration.

Introduction

Lithium-ion batteries (LIBs) currently dominate the secondary battery market for use in portable electronics and are widely regarded as a potential technology for electric vehicles and smart grids (*1*, *2*). Nevertheless, LIB cycling stabilities and energy densities are still far below those required for high-energy applications, so the development of rechargeable batteries with high energy density is urgently needed to meet the increasing demands for high-performance energy storage systems (*3*-*5*). Although LIB performance improvements have been achieved through the nano- and chemical engineering of both cathode and anode materials (*6*, *7*), these strategies usually increase material and battery manufacturing costs, as well as suffering from relatively poor scalability (*8*, *9*). Furthermore, the increasing demand for LIBs is accelerating our consumption of lithium, which may eventually render lithium unaffordable as a consequence of its relatively low abundance and the geopolitical challenges associated with its extraction (*10*).

The pursuit of high-energy density, long lifespan and low cost is at the heart of the development of next-generation rechargeable batteries. The deep exploitation of existing commercial materials is one of the most economical and effective alternatives, which also points to the way for the new battery design. On the other hand, the electrolyte in the existing LIB technique just functions as a medium for Li^+ cations transfer without extra capacity contribution. Under these circumstances, the potential contributions from anions in electrolyte are often neglected. For example, in the commercial $LiFePO_4$ (LFP) batteries (LFP as cathode and graphite as anode), Li-ions are reversibly extracted from the LFP cathode and inserted into graphite anode during charging, where only the Li^+ cations in the electrolyte are involved in the electrochemical reactions based on their "rocking-chair" operational mechanism, indicating no extra capacity contribution made by the sufficient and heavy electrolyte. Therefore, unlocking the latent energy of PF_6^- anions in the electrolyte might be a new breakthrough to further enhance the capacity and energy density of the existing LIBs.

Recently, the anion (such as PF_6^-, $AlCl_4^-$, and Cl^-) intercalation chemistry has been widely studied in dual-graphite batteries (DGBs), in which the anions from the electrolyte are intercalated/de-intercalated into/from the graphite cathode and the Li^+ cations are simultaneously inserted/extracted into/from the counter graphite electrode during charging/discharging, respectively (*11-13*). Differing from the LIB technique, the anions in the electrolyte are greatly utilized based on the working mechanism of DGBs. Benefiting from the low cost of "green" electrode material as well as the high operating voltage by anion intercalation, the DGBs have recently made great progress (*14-16*). Nevertheless, DGBs have been criticized for their "real" energy density. Because DGBs always need a large amount of electrolyte for anion intercalation, leading to the limited overall energy density (*17*). Moreover, the inherent drawbacks of graphite cathode, including limited layer space and serious structural deterioration due to repeating anion intercalation, result in their limited capacity (< 140 mA h g^{-1}) and unsatisfactory cycling stability, which also obstructs the widespread application of DGBs in the future (*18*).

In this work, the hybrid LFP/graphite electrodes with different graphite ratios were elaborately designed by a facile wet-milling strategy, in which the LFP particles were highly dispersed on the surface of the graphite. Compared to the pure LFP and graphite electrodes, the hybrid LFP/graphite-20% electrode delivered a high specific capacity, encouraging rate capability, and long-term cycling stability benifiting from the interaction of LFP and graphite through a staged Li^+ and PF_6^- de/intercalation mechanism. Unlike the operating mechanism of conventional LIBs and DGBs, Li^+ is reversible extracted from the LFP phase in the lower voltage range of 2.5 to 4.0 V, and subsequently PF_6^- from the electrolyte is reversibly intercalated into the graphite phase in the higher voltage range of 4.0 to 5.0 V in our hybrid battery, as illustrated in Fig. 1. Based on the staged de/intercalation mechanism, LFP/graphite-20% electrode only allows partial PF_6^- anions in the electrolyte to be involved in the electrode reactions due to the small proportion of graphite in this hybrid electrode, which takes full advantage of all parts of the battery. Compared to the LFP electrode, this low-cost hybrid electrode design of LFP/graphite improves the electronic conductivity of LFP by introducing graphite, facilitating the lithiation/delithiation process at lower voltage range (< 4.0 V). In turn, the delithiation process from the LFP also triggers *in-situ* generation of the cathode electrolyte interphase (CEI) protective layer on the hybrid electrode (Fig. S1, supporting information), which strengthens the structural integrity of the graphite for anion intercalation at high voltage (> 4.0 V). As a result, this hybrid LFP/graphite-20% electrode displays an excellent lifespan over 3500 cycles at 10 C, which is superior to the pure LFP and graphite electrode. Furthermore, the full-cell assembled with a graphite anode and hybrid LFP/graphite cathode delivers a higher energy density of ~176.7 Wh kg^{-1} (based on the whole battery) compared to the commercial graphite||LFP battery (~100−130 Wh kg^{-1}) and DGBs (~130 Wh kg^{-1}). This work presents a proof-of-concept hybrid electrode design capable of delivering a relatively high energy density using existing commercial electrode materials.

Results

Electrochemical performance of LFP, graphite and hybrid LFP/graphite electrode

As one of the most commonly used cathode candidates, olivine-typed LFP has been intensively investigated due to its excellent structural stability. Extraction of Li-ions from $LiFePO_4$ in one crystallographic orientation generates $FePO_4$ phase which has a similar stable structure even at a high voltage (*19*). Nevertheless, its poor electronic conductivity and low energy density resulting from its low output voltage (~3.5 V *vs.* Li^+/Li) have limited the further development of LFP battery. Recently, graphite has been studied as a cathode material that is able to be intercalated by the anions in the electrolyte at a high voltage (> 4.3 V *vs.* Li^+/Li). Such a high operating voltage is more likely to deliver a high energy density (*20*). Theoretically, a hybrid electrode could be created by introducing partial graphite into LFP, which would not only effectively accelerate the electronic conductivity of LFP but also enhance the out-put voltage of electrode due to PF_6^- anion intercalation into graphite at a high voltage. Accordingly, we synthesized the hybrid LFP/graphite electrode materials via a simple mechanical wet-milling of commercial LFP and graphite in different ratios (65:15, 60:20, 55:25, and 40:40, respectively). After wet-milling, the LFP particles with smaller size were highly dispersed on the surface of graphite in the sample of LFP/graphite mixture, as witnessed by scanning electron microscopy (SEM) (Figs. S2 and S3). Then, the X-ray diffraction (XRD) pattern of the mixture was measured, which was well accounted by both LFP and graphite structures (Fig. S4) (*21*).

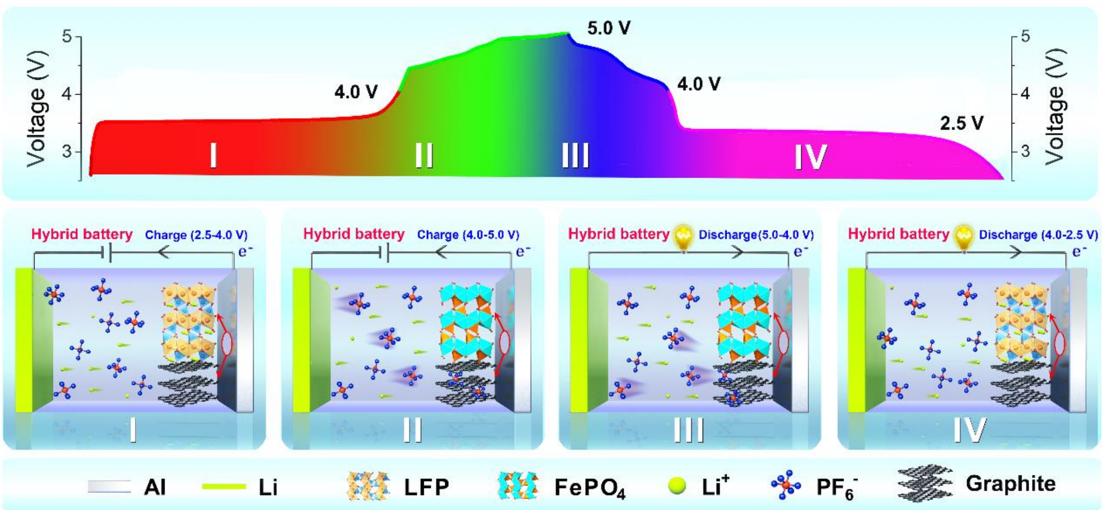

Fig. 1. Schematic illustration of the staged de/intercalated Li^+ and PF_6^- mechanism of the hybrid LFP/graphite in half-cell. Section **I**: initial charge from 2.5 to 4.0 V, in which Li^+ cations are extracted from the LFP. Section **II**: charge from 4.0 to 5.0 V, in which PF_6^- anions are intercalated into the graphite. Section **III**: discharge from 5.0 to 4.0 V, in which PF_6^- anions are extracted from the graphite. Section **IV**: discharge from 4.0 to 2.5 V, in which Li^+ cations are inserted into the $FePO_4$.

To validate the feasibility of the hybrid LFP/graphite electrodes, the electrochemical performances of LFP, graphite, and hybrid LFP/graphite electrodes in Li-based half-cells were measured in the electrolytes consisting of 1 M $LiPF_6$/ethylene carbonate (EC) + diethyl carbonate (DEC) + dimethyl carbonate (DMC) + 2% fluoroethylene carbonate (FEC) and 1 M $LiPF_6$/ethyl methyl carbonate (EMC) + 2% vinylene carbonate (VC), respectively. Fig. S5 shows that the LFP electrode at 1st cycle displays one charge/discharge plateau with a capacity of 143.5 mA h g^{-1} at 1 C (171 mA g^{-1}). This capacity is slightly lower than its theoretical value, mainly due to the polarization caused by its intrinsically poor conductivity (*22*, *23*). The pure graphite cathode shows several charge/discharge plateaus in 2.5−5.0 V with a reversible capacity of 114.2 mA h g^{-1} at 1 C (~140 mA g^{-1}), which is consistent with the reversible intercalation of PF_6^- into graphite (*18*, *24*). However, the initial Coulombic efficiency of graphite electrode is low (only ~50.0%). In comparison, the hybrid LFP/graphite electrodes exhibit a two-step charge process over the broadened voltage window of 2.5−5.0 V, corresponding to the process of Li^+ insertion/extraction (2.5−4.0 V) and PF_6^- intercalation/de-intercalation (4.0−5.0 V), respectively (Fig. S6). The optimal graphite proportion was also investigated in the hybrid electrode. Apparently, the hybrid LFP/graphite electrode with 15% graphite (LFP/graphite-15%) shows a small capacity contribution from graphite by anion intercalation (~22 mA h g^{-1}). Meanwhile, the small ratio of graphite has a limited impact on cutting down the cost of LFP cathode. With increasing the graphite ratio, the hybrid LFP/graphite-20% electrode (20% graphite) delivers a higher capacity of 154.0 mA h g^{-1} (based on the mass of LFP and graphite) and a higher initial Coulombic efficiency (77.5%) than other hybrid electrodes with 25% graphite and 40% graphite. This ratio of graphite (20% graphite) means the 1/4 of LFP active material was replaced, which should be a considerable contribution to reduce the cost of the cathode materials.

The charge-discharge profiles of different electrodes for the 2nd cycle are further compared in Fig. 2a. The LFP/graphite-20% electrode shows the charge-discharge curves containing charge-discharge characteristics of both LFP electrode and graphite electrode, indicating staged Li^+ extraction/insertion from/into LFP with the capacity of ~120 mA h g^{-1} and PF_6^- intercalation/deintercalation into/from graphite with the capacity of ~35 mA h g^{-1}, as the PF_6^- cannot intercalation into carbon black at the high voltage (Fig. S7). Benefiting from the staged de/intercalation of Li^+ and PF_6^-, the hybrid LFP/graphite-20% electrode delivers an energy density of 545.9 W h kg^{-1} (based on the active materials), significantly higher than 455.5 W h kg^{-1} obtained for the pure LFP material. Meanwhile, the Coulombic efficiency of the hybrid LFP/graphite-20% electrode is ~91.0%, also superior to ~70.9% obtained for the pure graphite electrode. The reversible sequential de/intercalation working mechanism of the hybrid LFP/graphite-20% electrode was also witnessed by the cyclic voltammetry (CV) measurement at 0.05 mV s^{-1} (Fig. 2b). An obvious peak at ~3.45 V and a broad peak above 4.0 V are assigned to the extraction of Li^+ from LFP and the intercalation of PF_6^- into graphite, respectively.

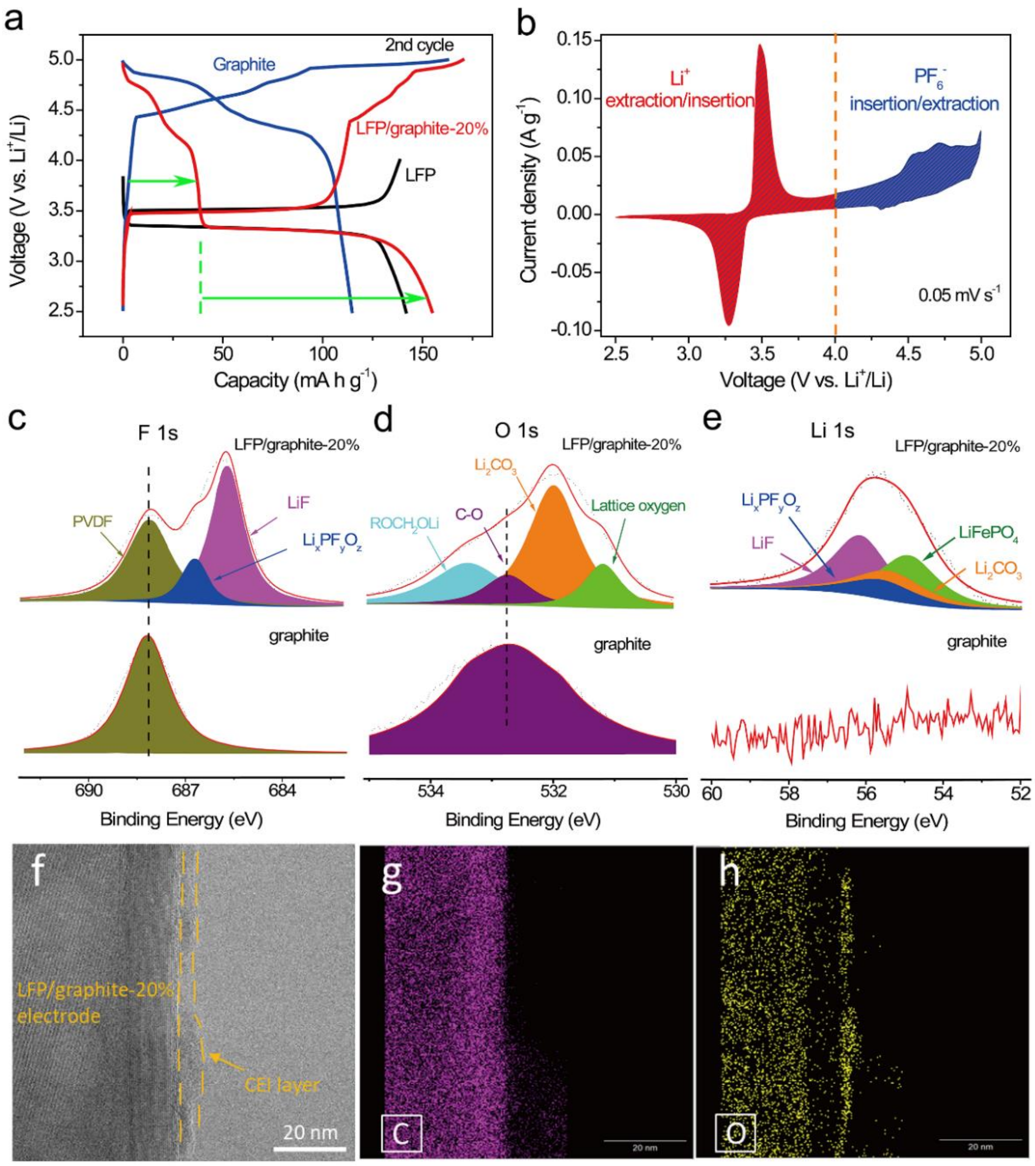

Fig. 2. Electrochemical characterization of different electrodes in half-cells at 1 C and CEI layer measurements. **a**, Charge-discharge voltage profiles during the 2nd cycle of LFP electrode in 1 M $LiPF_6$/EC + DEC + DMC + 2%FEC, graphite electrode in 1 M $LiPF_6$/EMC + 2% VC, and LFP/graphite-20% electrode in 1 M $LiPF_6$/EMC + 2% VC. **b**, Cyclic voltammograms of LFP/graphite electrode at 0.05 mV s^{-1}. X-ray photoelectron spectroscopy (XPS) spectra of LFP/graphite-20% (top) and pure graphite (bottom) electrodes after they were initially charged to 4.0 V: **c,** F 1s. **d,** O 1s. **e,** Li 1s. **F,** TEM image of LFP/graphite-20% electrode after it was initially charged to 4.0 V, **g,** the mapping of C element. **h,** the mapping of O element.

According to previous reports (*20*, *25*), the pure graphite cathode in DIBs cannot generates an integrated and stable CEI layer on its surface during the charge-discharge process. Could the staged working mechanism of hybrid LFP/graphite electrode help to *in-situ* build a stable CEI layer on the whole electrode within the low voltage range of 2.5−4.0 V? Here, X-ray photoelectron spectroscopy (XPS) was conducted to study the surface chemistry of the pure graphite and hybrid LFP/graphite-20% electrode after initially charging to 4.0 V, as presented in Fig. 2c-e, respectively. Compared to the pure graphite electrode, the hybrid LFP/graphite-20% shows the typical CEI components, such as $ROCH_2OLi$, Li_2CO_3, LiF, and $Li_xPF_yO_z$ (*26*). To be precise, three deconvoluted peaks in the F 1s spectrum for the LFP/graphite-20% sample are found at approximately 685.5, 688.0 and 686.6 eV (Fig. 2c), corresponding to polyvinylidene difluoride (PVDF), $Li_xPF_yO_z$, and LiF, respectively (*27*). The main LiF ingredient is probably derived from the decomposition of $LiPF_6$ to form HF, which reacts with the LFP component to form LiF (*28, 29*). In contrast, the graphite electrode just shows the binding energy of PVDF without any other F-containing compounds, indicating that no obvious CEI layer was formed on the pure graphite electrode, as discussed elsewhere (*25*). Similarly, the O 1s spectrum of LFP/graphite-20% can be deconvoluted into four peaks centred at approximately 533.5, 532.7, 532.0, and 531.0 eV (Fig. 2d), which are ascribed to $ROCH_2OLi$, C-O, Li_2CO_3, and lattice oxygen, respectively (*30*), whereas only the C-O peak can be detected at about 532.7 eV in the pure graphite sample. More obviously, the LFP/graphite-20% sample shows strong binding energy of in the Li 1s XPS spectrum with the deconvolution of LiF, $Li_xPF_yO_z$ and Li_2CO_3 (Fig. 2e) (*26*). No obvious Li signal was detected in the pure graphite sample, further indicating that there was no CEI protective layer on its surface. Moreover, the CEI layer on the LFP/graphite-20% electrode was also clearly observed by transmission electron microscopy (TEM), as illustrated in Fig. 2f. It revealed that the CEI layer was uniformly coated on the hybrid electrode, as convinced by the energy-dispersive X-ray spectroscopy mapping (EDX, Fig. 2g-h). The O element exhibits a homogeneous and opposite distribution from the C element, also demonstrating the uniform CEI coating on the electrode material. However, no clear CEI layer was found on the graphite sample (Fig. S8), which is in accordance with the XPS results. Through these comparisons, it is clear that the staged working mechanism of hybrid electrode facilitates to build an integrated CEI protective layer on the electrode surface within the low voltage range of 2.5−4.0 V.

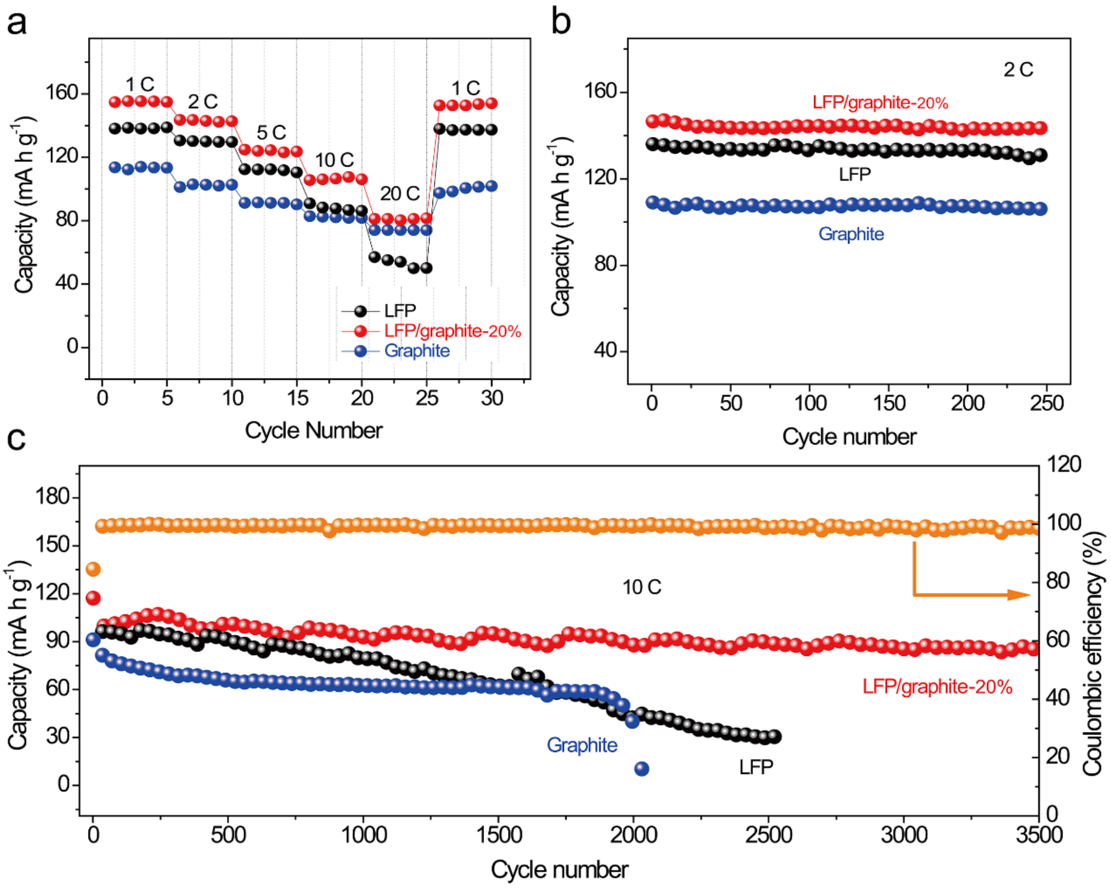

Fig. 3. Electrochemical comparison of different electrodes in half-cells. **a**, Rate capability of LFP, graphite, and hybrid LFP/graphite-20% electrodes at various current rates. **b**, Cycling performance of three electrode at 2 C for 250 cycles. **c**, Long-term cycling stabilities of three electrodes at 10 C over 3500 cycles and the Coulombic efficiency of hybrid electrode.

The rate capabilities of the pure LFP, graphite, and hybrid LFP/graphite-20% electrodes at various rates from 1 to 20 C are presented in Fig. 3a. Graphite electrode delivered a capacity of 71.8 mA h g^{-1} with capacity retention of ~63.1% when the current rate was increased to 20 C, which is consistent with the expected high rate capability of graphite for PF_6^- storage (*31*). The decreased capacity of ~50.7 mA h g^{-1} (only ~35.7% capacity retention) for LFP electrode at 20 C indicates its poor rate capability, likely arising from sluggish Li^+ diffusion (*32*). In contrast, the hybrid LFP/graphite-20% electrode delivered a high capacity of 78.7 mA h g^{-1} remained even at 20 C (~51.0% capacity retention), and the capacity returned back to its initial value when the current density was reduced to 1 C, suggesting the excellent reversibility of both Li^+ and PF_6^- storage in the hybrid material. In addition to the effects of the CEI protective layer, the density functional theory (DFT) calculations were performed to study the impacts of the barriers of Li^+ diffusion in LFP and PF_6^- diffusion on the rate capability of the hybrid electrode (Fig. S9). According to previous reports, Li^+ preferentially migrates along the [010] direction in LFP, and the energy barrier was calculated to be 0.34 eV, which is similar to that reported elsewhere (*33*). PF_6^- is found to preferentially migrate along the [100] direction in graphite and its energy barrier was calculated to be 0.22 eV (Fig. S9b-c), lower than that of Li^+ in LFP phase, which indicates the easier, and therefore likely faster, diffusivity of PF_6^- in graphite than that of Li^+ in LFP phase. The results also agree well with the higher rate capabilities of the hybrid LFP/graphite-20% and pure graphite electrodes compared with that of pure LFP material.

The cycling stability of the three electrodes was assessed at a low current rate of 2 C, as shown in Fig. 3b. After 250 cycles, the corresponding percentage capacity retention values were found to be ~95.6%, ~97.0, and ~97.1% for pure LFP, graphite and hybrid LFP/graphite-20% electrodes, respectively, suggesting that they are electrochemically stable at the low current rate. After cycling, the morphology of the hybrid LFP/graphite-20% electrode was studied by scanning transmission electron microscopy (STEM), as shown in Fig. S10. The LFP particles are homogeneously dispersed on the graphite sheets, in turn, the graphite sheets preserve the integrity of the hybrid electrode by acting as the structural supports for the LFP particles, facilitating the long-term cycling stability of the hybrid electrode. Subsequently, the cycling stability of three electrodes was further compared at the high rate of 10 C (Fig. 3c). Clearly, the pure LFP electrode shows serious capacity decay with the capacity retention of ~34.1 %

after 2500 cycles. The main reason is likely to be its limited electronic and ionic conductivity, resulting in a huge energy barrier for the diffusion of electrons and Li^+ ions at a high rate, which induces the shedding of active material from the current collector during the long-term rapid Li^+ insertion/extraction process. The serious shedding is evidenced by the photographs of LFP electrode stripped out of the battery after 2500 cycles (Fig. S11a-b). The pure graphite electrode shows the severe capacity attenuation after approximately 2000 cycles, which is mainly attributed to the collapse of the graphite structure after long-term anion intercalation. The collapse of the graphite results in the completely detachment of active material from the current collector (Fig. S11c-d). In strongly comparison, the LFP/graphite-20% electrode exhibits an ultra-long lifespan of 3500 cycles with a capacity retention of ~78.5 % at 10 C, which mainly benefits from the enhanced conductivity of LFP component as well as the reinforced structural stability by generating a CEI protective layer. The Raman spectra provides an intuitive comparison of the structure changes of the cycled hybrid LFP/graphite-20% and pure graphite electrodes, as shown in Fig. S12. Notably, the intensity ratios of the D to the G band (I_D/I_G) for pure graphite remarkably increased after 2000 cycles, indicating that the aggravated degree of disordered in the graphite due to long-term anion intercalation. However, the intensity ratios of I_D/I_G for the hybrid LFP/graphite-20% before and after cycling are similar, which suggests the well-maintained graphitic structure benefiting from the protection from CEI layer.

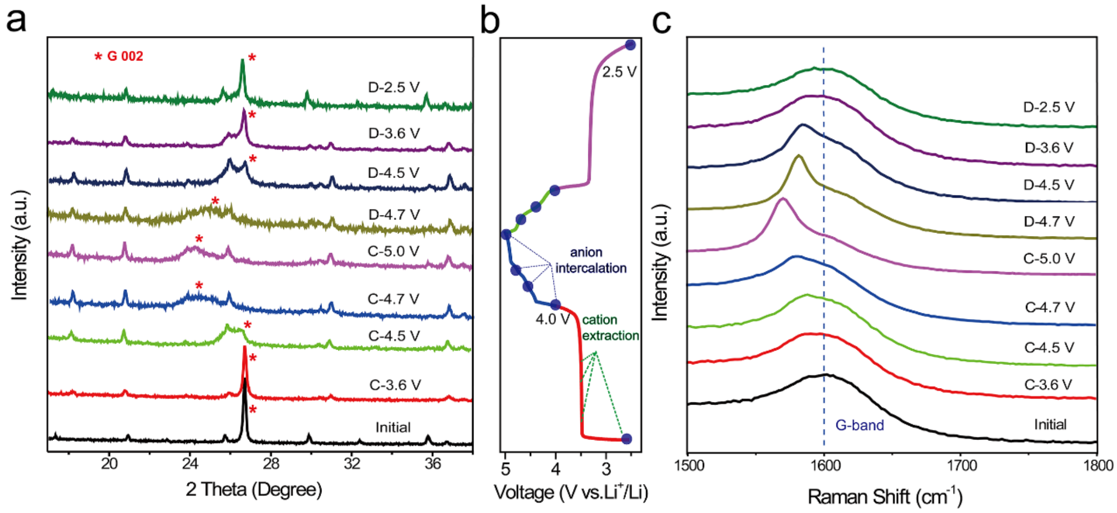

Fig. 4. *Ex-situ* techniques used to study the working mechanism of the hybrid electrode. **a,** *Ex-situ* XRD patterns of LFP/graphite-20% electrodes extracted from cells equilibrated at 3.6, 4.5. 4.7, and 5.0 V on charge (labelled C) and 4.7, 4.5, 3.6, and 2.5 V on discharge (labelled D). **b,** The corresponding charge-discharge profile. **c**, *Ex-situ* Raman spectra, demonstrating the reversible shift of the G-band feature as a result of the intercalation/de-intercalation of PF_6^-.

The working mechanism of hybrid electrode

To comprehensively understand the working mechanism of the hybrid LFP/graphite-20% electrode in half-cells, the *operando* synchrotron X-ray powder diffraction (XRPD), *ex-situ* X-ray diffraction (XRD), Raman spectroscopy and XPS measurements were conducted. As illustrated in Fig. S13, the reflections of LFP was found to shift upon charging, however, no 002 reflection of graphite was observed. The main reason should be assigned to the transmission mode of the synchrotron beamline. To gain the detailed evolution information of graphite electrode upon charging/discharging of LFP/graphite-20% electrode, the *ex-situ* XRD with reflection mode was further studied. After charging to 3.6 V, new reflections at 18.1°, 20.6°, and 30.8° appear, which were indexed to heterosite ($FePO_4$) 200, 101, and 020 reflections (Fig. 4a), respectively, with no reflections observable from LFP, indicating that LFP is fully transformed into the heterosite phase (*23*). Upon further charge from 3.6 to 5.0 V, the reflections from $FePO_4$ remain unchanged, indicating the stability of this phase at high voltage. Additionally, reflections arising from graphite are also observed. Notably, the graphite 002 reflection is shifted to lower angles and is lower in intensity than that observed at 3.6 V, consistent with the intercalation of PF_6^- and indicating expansion of the *c* lattice parameter and associated loss of coherency, respectively (*34*). Anion intercalation was also evidenced by the *ex-situ* XPS measurements (Fig. S14). The XPS curves show features at ~688.3, 531.2, 284.6, and 132.8 eV, corresponding to F 1s, O 1s, C 1s, and P 2p photoemission lines, respectively. After charging to 4.6 V, the intensities of the F 1s and P 2p photoemission lines increase substantially, with the concentration of F and P increasing to 18.6 and 7.2 wt.%, respectively (Fig. S15). On discharging to 3.6 V, the hybrid material exhibits a graphite 002 reflection position that is close to the initial state (Fig. 4b), suggesting the excellent reversibility of the PF_6^- insertion. The corresponding *ex-situ* Raman spectra (Fig. 4c) reveal that the characteristic G-band arising from the graphite at ~1590.7 cm^{-1} remains unchanged upon charge to 3.6 V (*35*). Samples further charged to 5.0 V show a red-shift of the G-band feature compared with the samples at 3.6 V, further evidencing the intercalation of PF_6^- into the graphite at this voltage, in good agreement with the XRD and XPS results. Taken together, the overall electrochemical reaction mechanism of this hybrid LFP/graphite electrode consists of a reversible LFP phase transformation in the low voltage region and the reversible intercalation of PF_6^- into graphite in the high voltage range, as described by:

$$\mathrm{LiFePO_4} \leftrightarrow \mathrm{Li^+} + \mathrm{e^-} + \mathrm{FePO_4}\ (2.5\ < \mathrm{V} < 4.0) \qquad (1)$$

$$x\mathrm{C} + \mathrm{PF_6}^- \leftrightarrow \mathrm{C}_x\mathrm{PF_6} + \mathrm{e^-} (4.0 <\ \mathrm{V} < 5.0) \qquad (2)$$

Full-cell measurements

To further explore the practical implementation of the hybrid electrodes, full-cells were constructed with LFP/graphite-20% cathode and graphite anode, respectively, as illustrated in Fig. 5a. The typical charge/discharge profiles of graphite electrode in half-cell, LFP/graphite-20% in half-cell, and the graphite||LFP/graphite full-cell were collected at 0.5 C (Fig. 5b).

Similar to the hybrid LFP/graphite-20% electrode in a half-cell, the charge/discharge curves of the graphite||LFP/graphite full-cell also shows a two-step process over the broadened voltage window of 2.3−4.8 V, suggesting its operating mechanism based on the staged de/intercalation of cations and anions. And a high initial discharge capacity of ~150.7 mA h g^{-1} was obtained at 0.5 C, whose effectiveness is demonstrated further by powering 6 blue light-emitting diodes (3 V) (Fig. 5c) and a digital thermometer and hygrometer (Fig. S16). Furthermore, this full-cell displays an encouraging cycling stability at 5 C with the capacity retention of ~90.1% after 140 cycles (Fig. 5d). Generally, energy and power density, cycle life, and affordability are the critical parameters in determining the commercial viability of an energy storage device. Notably, the partial replacement of LFP by relatively cheap graphite in the hybrid battery increases all of these. An impressive energy density of ~176.7 W h kg^{-1} was attained for the graphite||LFP/graphite battery at a power density of ~106.1 W kg^{-1} (Table S1), which is substantially higher than that of current graphite||LFP batteries which typically deliver ~100−130 W h kg^{-1}, DGBs (~130 W h kg^{-1}) and other devices (Fig. S17) (*36*). The low overall cost and high energy density of this hybrid full-cell also offers substantial commercial potential in the future energy applications, such as the grid.

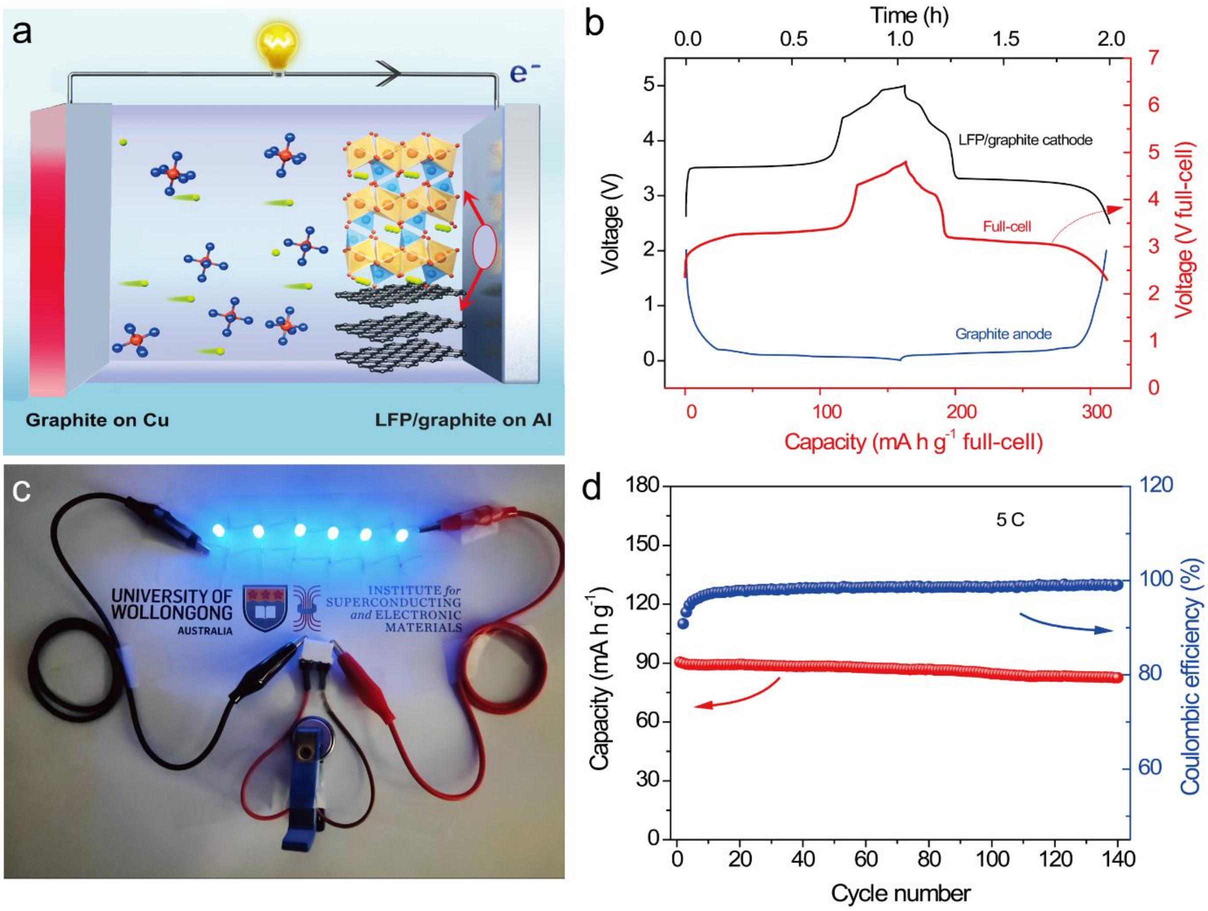

Fig. 5. Electrochemical performance of a typical graphite||LFP/graphite full-cell. **a**, Schematic illustration of graphite||LFP/graphite full-cell. **b**, Typical charge-discharge voltage profiles at a current rate of 0.5 C. **c**, The full-cell powers six blue light-emitting diodes (3 V). **d**, Cycling stability at 5 C over 140 cycles with the corresponding Coulombic efficiency.

In order to further study the operating mechanism of the hybrid LFP/graphite electrode in the full-cell, *in operando* neutron powder diffraction (NPD) was performed. The graphite anode, however, would have an influence on the 002 reflection of graphite cathode during the charge-discharge process. Therefore, graphite anode should be replaced by other anode candidates to avoid such an impact on the graphite cathode. Due to its alloying reaction with Li, the Al foil has been reported as an anode candidate in dual-ion batteries by Tang and co-workers.(*14*) Building an Al||LFP/graphite full-cell would be an easy way to study the working mechanism of hybrid LFP/graphite in a full-cell. First, the electrochemical behaviour of the Al foil was examined in a half-cell (Fig. S18). It reveals a relatively low charge plateau at ~0.45 V due to the formation of a LiAl alloy, as convinced by *ex-situ* XRD measurements (Fig. S19), which suggests that Al could be a good anode candidate. An Al||LFP/graphite pouch-cell was assembled as shown in Fig. S20a. During charging-discharging process, o*perando* NPD results were collected in Fig. S20b. Reflections from LFP, $FePO_4$, and graphite phases are clearly seen, and over the voltage range of 2.2−3.5 V, the expected two-phase behaviour of LFP and $FePO_4$ is observed (*19*). Within this voltage window, the graphite 002 reflection located at 41.5° remains unchanged, indicating no electrochemical activity. In the subsequent charge process from 3.5 to 4.6 V, the main reflection of graphite gradually shifts to lower angles, indicating expansion of the *c* lattice parameter, as is consistent with a solid-solution reaction, since PF_6^- intercalates between the layers of the graphite structure (*37*). Single-peak fitting using these data revealed the evolution of the interlayer spacing of the $(PF_6)C_x$ phases during these processes (Fig. 6a) (*37*). The spacing gradually increases from 3.35 Å to 3.50 Å during the charge to 4.6 V, which was further verified by *ex-situ* high resolution TEM (HRTEM) measurements (Fig. 6b-c). Correspondingly, a uniform distribution of relatively highly concentrated F element is found. During the discharge from 4.6 to 3.5 V, the interlayer spacing returns to 3.35 Å, indicating the good reversibility of anion intercalation. On the following discharge to 2.2 V, HRTEM images of LFP/graphite extracted from the cells showed lattice fringes with a spacing of ~3.35 Å (Fig. 6d), indicating that the PF_6^- had been fully extracted from the graphite, as corroborated by the relatively low concentration of F element. These results demonstrate that the hybrid electrode design is available with a staged de/intercalation mechanism in a full-cell.

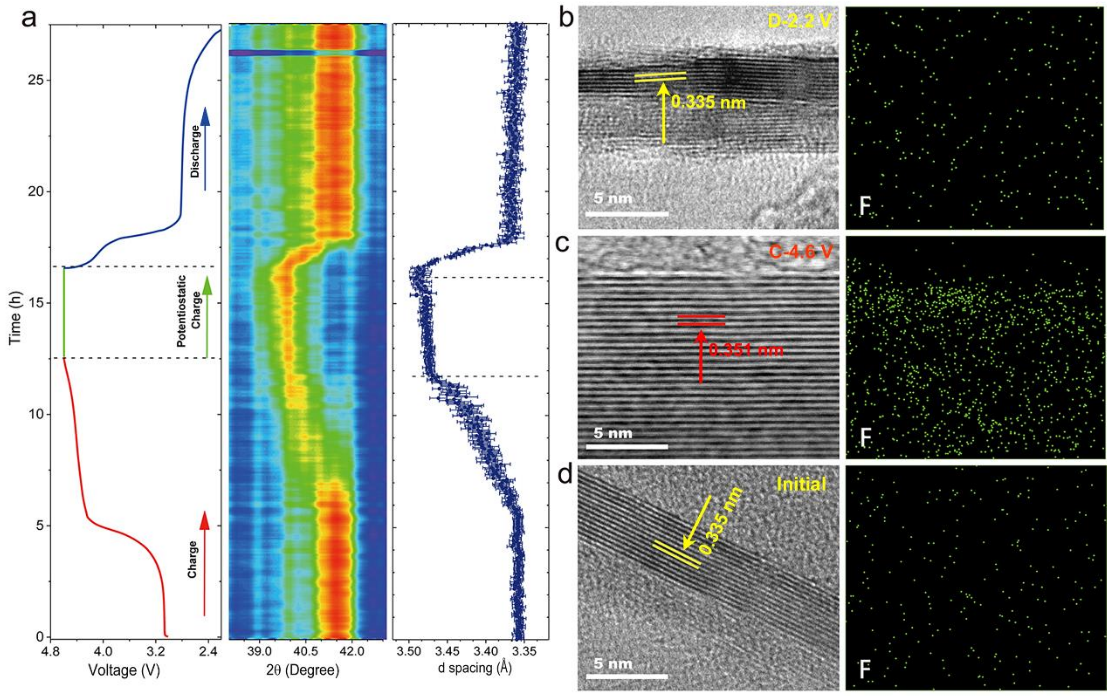

Fig. 6. NPD and HRTEM revealing the operational mechanism of the Al||LFP/graphite pouch-cell**. a,** *In operando* NPD results with intensity shown in color of the $(PF_6)C_x$ (002) reflection (middle), with the *d* spacing derived from Rietveld refinement (right) and the charge-discharge profile (left). **b, c, d,** HRTEM images (left) showing the distribution of F (right) in LFP/graphite (**b**) at the initial state of charge, (**c**) at charge to 4.6 V, and (**d**) at discharge to 2.2 V.

Opportunities and challenges of the hybrid battery

Our rechargeable battery concept using the hybrid electrode design has some unique features and advantages compared to traditional LIB technique. The "rocking chair" mechanism was revolutionized by the staged de/intercalation mechanism of Li^+ cations and PF_6^- anions. By this means, the role of the electrolyte would be fully developed, which not only provides a medium for Li^+ transfer but also allows the PF_6^- anions to participate in the electrode reaction. Such a working mechanism improves the average out-put voltage and capacity of the battery, yielding enhanced energy density. Furthermore, building a hybrid electrode consisting of highly-dispersed LFP on graphite not only increases the electronic conductivity of the LFP phase, but also reinforces the structurally stability of graphite component by generating a protective CEI layer at low voltage window, which benefits to improve the rate capability and long-term cycling stability. Compared to the LFP material, the graphite is metal-free and "green", which enables the hybrid LFP/graphite electrode to offer certain advantages compared to the LFP cathode in terms of the overall cost, environmental friendliness, and metal consumption, especially of Li element. Theoretically, the hybrid electrode design could also be extended to other traditional cathode with low working voltage and high stability at high voltage, such as $LiMn_2O_4$ cathode. However, this hybrid design may not suitable for the cathode whose structure is not reversible at the high working voltage range, such as $LiCoO_2$ cathode.

Nevertheless, our hybrid battery design is still far from fulfilling the ambition to replace the current market of commercial LIBs currently, as it still faces several challenges as follows. For the hybrid LFP/graphite-20% electrode, the initial Coulombic efficiency is still relatively low (about 77.5%, and ~91.0% for the second cycle). The limited initial Coulombic efficiency of the hybrid electrode can be mainly assigned to its anion intercalation behavior (~4.2 V *vs.* Li^+/Li), which may exceed the stable window of conventional carbonate electrolytes (*38*). Thus, using an ionic liquid (albeit expensive) (*18*), developing new electrolyte additives and stable solvents or constructing an artificial solid electrolyte interphase layer on the electrode could be the effective strategies to suppress the decomposition of electrolyte and further improve the Coulombic efficiency (*20*). Another issue is that the specific capacity improvement for the proposed hybrid LFP/graphite-20% cathode is limited (approximately 9%) compared to the LFP electrode, although graphite brings high operating voltage and high conductivity for the hybrid electrode. Actually, the commercial LFP material has contained amorphous carbon materials to enhance its electrical conductivity. Unlike the graphite, however, the amorphous carbon materials cannot contribute to the capacity due to the lack of sites for anion intercalation, which has been confirmed in Fig. S7. Further replacing (or partially replacing) the amorphous carbon in commercial LFP electrode by graphite during the manufacturing process could not only reduce the "dead weight" of the electrode, but also allow more PF_6^- anions to intercalate into the graphite, thus further improving the capacity and energy density. Last but not least, a comprehensive investigation focused on the development of a suitable electrolyte still needs to be conducted to enhance the overall performance (especially for the full-cell). In addition to the electrolyte consisting of 1 M $LiPF_6$/EMC + 2% VC, an electrolyte consisting of 1 M $LiPF_6$/EC + DEC + DMC + 2% FEC has been applied with the graphite cathode and the hybrid LFP/graphite-20% electrodes in our work, however, the capacity and cycling stability are very limited, as shown in Fig. S21. The concentration of our current electrolyte is low (1 M), which might be harmful for the energy density of the hybrid battery, as the anions in the electrolyte need to involve in the electrode reaction based on its staged cation and anion de/intercalation mechanism. Therefore, more studies on the electrolyte are still highly desirable for further development of the hybrid system, such as developing highly-concentrated electrolytes. The utilization of high-concentrated electrolytes with should be a simple and suitable strategy to optimize the reversibility of anion intercalation and further enhance the electrochemical properties (such as Coulombic efficiency and energy density) of our hybrid batteries. One has to keep in mind, however, that the substantially high demand for salts would introduce high cost as well as the high viscosity of the electrolyte, so it is adjudged wise to find right balance for achieving the low cost and advanced electrochemical performance.

Discussion

In this work, a proof-of-concept study of LFP/graphite hybrid electrode was conducted in half-cells and full-cells, which pushes the limitations of the "rocking chair" mechanism by unlocking the anion contribution. Compared to pure LFP and graphite electrodes, our hybrid LFP/graphite-20% electrode delivers an encouraging overall electrochemical performance, including enhanced energy density, rate capability, and life span, benefiting from the interaction of LFP and graphite. Specifically, the hybrid LFP/graphite-20% electrode in a half-cell exhibits an excellent stability over 3500 cycles at a high rate of 10 C. More importantly, when the full-cell was assembled using LFP/graphite-20% cathode and graphite anode, an impressive energy density approaching ~176.7 W h kg^{-1} was attained, higher than that of graphite||LFP batteries (~100−130 W h kg^{-1}) and DGBs (~130 W h kg^{-1}). This hybrid design offers significant advantages in terms of overall cost as well as energy density, and is extendable to other conventional electrode materials. Nonetheless, further improvement of battery performance, including optimization of the electrode and battery configuration, selection of compatible electrolyte, and strategies for improving the initial Coulombic efficiency must be systematically devised in order to realize the real application of this hybrid system.

Methods

Materials. $LiFePO_4$ (LFP, ~1.35 um), Li foil (thickness ~100 μm), expanded graphite (D50, 19.0-23.0 um), and Al foil (thickness ~25 μm) were purchased from Shenzhen Kejing Star Technology. PVDF binder, conductive carbon black, N-methyl-2-pyrrolidone (NMP), ethylene carbonate (EC), diethyl carbonate (DEC), dimethyl carbonate (DMC), fluoroethylene carbonate (FEC), ethyl methyl carbonate (EMC), vinylene carbonate (VC), and $LiPF_6$ (battery grade, 99.99%) were purchased from Sigma-Aldrich Co. All chemicals were used directly without further processing. The hybrid LFP/graphite materials were prepared by wet-milling of LFP and graphite in ethanol with different weight ratio of 65:15, 60:20, 55:25, and 40: 40, respectively. The ball-milling process was conducted for 8 h using zirconia milling beads under a milling speed of 450 rpm in a planetary QM-1SP2 mill.

Characterization. The crystalline structure of the obtained materials was investigated by X-Ray Diffraction (XRD, GBC MMA diffractometer) with Cu Kα radiation. X-ray Photoelectron Spectroscopy (XPS) was performed on a VG Multilab 2000 (VG Inc.) photoelectron spectrometer using monochromatic Al Kα radiation with background pressure below 2×10^{-6} Pa. All binding energies were referenced to the C 1s peak at 284.8 eV of the surface adventitious carbon. The morphologies of the LFP, graphite, and LFP/graphite were investigated by field emission Scanning Electron Microscope (SEM, JEOL JSM-7500FA). The details of the crystal structure at high resolution and the corresponding energy dispersive spectroscopy (EDS) mapping were further examined by Scanning Transmission Electron Microscope (STEM, JEOL JEM-ARM200F), which was conducted at 200 kV. Raman spectroscopy (Jobin Yvon HR800) using a 10 mW helium/neon laser at 632.8 nm was employed to characterize the D-band and G-band of graphite during charging-discharging processes.

Electrochemical measurements. Electrochemical testing was conducted using CR2032 coin-type cells, which were assembled in an argon-filled glove box with oxygen and moisture levels below 0.01 ppm. Working electrodes were prepared by mixing the electrode materials (LFP, graphite, LFP/graphite), carbon black, and PVDF in a weight ratio of 80:10:10, and adding several drops of NMP solvent to form homogeneous slurries. The as-obtained slurries were spread onto Al foil and dried at 120 °C for 12 h in a vacuum oven. By this mean, the specific ratio of LFP: graphite: active carbon: PVDF in different LFP/graphite electrodes is 65:15:10:10 (LFP/graphite-15%), 60:20:10:10 (LFP/graphite-20%), 55:25:10:10 (LFP/graphite-25%), and 40:40:10:10 (LFP/graphite-40%), respectively. In addition, the LFP-60% electrode was prepared using the weight ratio LFP: carbon black: PVDF = 60:30:10. Electrochemical measurements of half-cells were carried out using Li metal as counter and reference electrode and glass fiber (Whatman) as the separator in electrolyte composed of 1 M $LiPF_6$ electrolyte salt in either EC:DEC:DMC (1:1:1 v/v) + 2% FEC or EMC + 2% VC. Electrochemical measurements of full-cells were carried out using graphite as counter and reference electrode with an electrolyte consisting of 1 M $LiPF_6$ in EMC + 2% VC. Cyclic voltammetry was conducted on a VMP-3 electrochemical workstation at a scan rate of 0.05 mV s^{-1}. The assembled cells were galvanostatically charged and discharged at different current densities using a Land CT2001A battery tester. The graphite||LFP/graphite full-cell was assembled using hybrid LFP/graphite electrode (on Al foil) as cathode and graphite electrode (on Cu foil) as anode with the capacity ration of cathode and anode is 1:1.1. Before assembling the full-cell, both cathode and anode were cycled ten times in Li-based half-cell.

***Operando* synchrotron (XRPD):** The synchrotron cells with a hole on the cases was used for operando XRPD measurements of LFP/graphite-20% sample, which is similar to the coin cells used in electrochemical testing. The cell was galvanostatically charged in 2.5–5.0 V (*vs.* Li^+/Li) at 0.18 mA (~200 mA g^{-1}). The XRPD patterns were collected every 15 min using a MYTHEN micro-strip detector during the charge process. The used wavelength was detected to be 0.6887 Å using a LaB_6 NIST SRM 660b.

***Operando* NPD.** A customized pouch cell with the Al||LFP/graphite full-cell configuration was prepared using the hybrid LFP/graphite, Al foil and Immobilon-P PVDF separator (Millipore). The electrodes were cut into 1 × 5 cm^2 strips, and the pouch cell was prepared by stacking 25 electrode/separator/electrode assemblies with a parallel connection, which then was wrapped in polypropylene-coated Al foil. Both electrolyte injection and heat-sealing were conducted in an Ar-filled glovebox. During NPD measurements, the Al||LFP/graphite pouch cell was first charged to 4.6 V, subsequently held at 4.6 V for 4 h, and then discharged to 2.2 V at 0.1 C using an Autolab PGSTAT302N (*39*). NPD data were simultaneously collected on the high-intensity neutron powder diffractometer WOMBAT at the Open Pool Australian Light-water (OPAL) research reactor facility at ANSTO (*40*). A neutron beam with a wavelength of 2.417(2) Å was used, as determined using the $La^{11}B_6$ NIST standard reference material 660b. The diffraction data were continuously collected with an exposure time of 3 min per pattern in the range of $16° < 2\theta < 136°$. NPD data correction, reduction, and visualization were undertaken using the LAMP software package (*41*). GSAS-II was used for sequential peak fitting of the main reflection of graphite in the NPD data (*42*).

DFT Calculations. The Vienna Ab initio simulation package (VASP 5.4.4) was employed for all calculations using the generalized gradient approximation plane-wave projector-augmented wave method of Perdew–Burke–Ernzerhof (GGA-PBE) with the cut-off energy of the plane wave basis set to 450 eV (*43, 44*). Optimized structures were obtained by fully relaxing all atomic positions and cell parameters until the force on each atom was smaller than 0.02 eV/Å and energies converged to within 5×10^{-5} eV per atom. A climbing-image nudged elastic band (cNEB) method was used to calculate the energy required for PF_6^- to move between sites in graphite and Li^+ to move between sites in LFP.

For LFP, the Hubbard-term corrected GGA (GGA+U) theory was adopted to account for the strong on-site coulomb interaction of localized electrons of the 3d transition metal Fe with the U value of 5.3. A 2 × 2 × 1 supercell was used to calculate the energy of the on-dimensional migration of a Li vacancy (V_{Li}) along the [010] direction of LFP (*45*). The binding energy of Li (ΔE_{Li}) was calculated to be -3.51 eV from:

$$\Delta E_{Li} = E_{\mathrm{LiFePO_4}} - E_{\mathrm{FePO_4}} - E_{\mathrm{Li}}$$

where $E_{\mathrm{LiFePO_4}}$, $E_{\mathrm{FePO_4}}$ and E_{Li} are the calculated energies of LFP, $FePO_4$, and Li metal, respectively.

For PF_6^- intercalated graphite, the system was represented by a 4 × 4 × 2 supercell containing 128 carbon atoms, which formed 4 layers of graphite, and one PF_6^- anion located in one of the four interspaces. A 2 × 2 × 1 k-point grid within the Monkhorst-Pack scheme was used to sample the Brillouin zone of the system (*46*). Starting with several possible testing structures, we performed full relaxation and then calculated their corresponding binding energies. We chose the one with the largest binding energy as the most stable structure, based on which, we thereafter performed the cNEB calculation. For the PF_6^- intercalated graphite system, the binding energy of PF_6^- ($\Delta E_{\mathrm{PF_6}}$) was calculated to be -2.26 eV by:

$$\Delta E_{\mathrm{PF_6}} = \mathrm{E}_{\mathrm{C_{128}PF_6}} - \mathrm{E}_{\mathrm{C_{128}}} - \mathrm{E}_{\mathrm{PF_6}}$$

where $\mathrm{E}_{\mathrm{C_{128}PF_6}}$, $\mathrm{E}_{\mathrm{C_{128}}}$ and $\mathrm{E}_{\mathrm{PF_6}}$ are the calculated energies of $C_{128}PF_6$, C_{128}, and PF_6, respectively.

Acknowledgements

This research has been carried out with the support of the Australian Research Council (ARC) through a Discovery Project (DP170102406) and Future Fellowships (FT150100109, FT160100251) are gratefully acknowledged. Work at Argonne National Laboratory was supported by the U. S. Department of Energy (DOE), Office of Energy Efficiency and Renewable Energy, Vehicle Technologies Office. Argonne National Laboratory is operated for DOE Office of Science by UChicago Argonne, LLC, under contract number DE-AC02-06CH11357. The Electron Microscopy Centre (EMC) at the University of Wollongong is owed thanks for the electron microscopy characterizations, as well as Dr. Xiaohe Song (National University of Singapore) due to his support for DFT calculations, and Dr. Tania Silver for critical reading of the manuscript. The authors are also grateful to the staff of the Australian Centre for Neutron Scattering for their operational support during *in operando* NPD measurements.

Author contributions

J.H. conducted the experiments, analysed the data, and wrote the manuscript. F.Y. and H.H. helped to conduct the electrochemical measurements. S.Z. and Y.L. performed the SEM and

TEM characterizations. W.P., V.K.P., and C.D. conducted the NPD tests and analysis. J.L revised the manuscript. G.X. and Z.G. conceived and supervised the project.

References

1. B. Dunn, H. Kamath, J. M. Tarascon, Electrical energy storage for the grid: A battery of choices. *Science* **334,** 928-935 (2011).
2. X. G. Yang, G. Zhang, S. Ge, C. Y. Wang, Fast charging of lithium-ion batteries at all temperatures. *Proc. Natl. Acad. Sci. U.S.A.* **115,** 7266-7271 (2018).
3. J. B. Goodenough, K. S. Park, The li-ion rechargeable battery: A perspective. *J. Am. Chem. Soc.* **135,** 1167-1176 (2013).
4. H. Chen *et al.*, Ultrafast all-climate aluminum-graphene battery with quarter-million cycle life. *Sci. Adv.* **3,** eaao7233 (2017).
5. S. Guo *et al.*, SiO_2- enhanced structural stability and strong adhesion with a new binder of konjac glucomannan enables stable cycling of silicon anodes for lithium- ion batteries. *Adv. Energy Mater.* **8,** 1800434 (2018).
6. J. Hao *et al.*, Heterostructure manipulation via in situ localized phase transformation for high-rate and highly durable lithium ion storage. *ACS Nano* **12,** 10430-10438 (2018).
7. F. Yang *et al.*, Yolk–shell structured FeP@C nanoboxes as advanced anode materials for rechargeable lithium- /potassium- ion batteries. *Adv. Funct. Mater.* **29,** 1808291 (2019).
8. D. Larcher, J. M. Tarascon, Towards greener and more sustainable batteries for electrical energy storage. *Nat. Chem.* **7,** 19-29 (2015).
9. R. Schmuch, R. Wagner, G. Hörpel, T. Placke, M. Winter, Performance and cost of materials for lithium-based rechargeable automotive batteries. *Nat. Energy* **3,** 267-278 (2018).

10. N. Nitta, F. Wu, J. T. Lee, G. Yushin, Li-ion battery materials: present and future. *Mater. Today* **18,** 252-264 (2015).

11. T. Placke *et al.*, Dual-ion cells based on anion intercalation into graphite from ionic liquid-based electrolytes. *Z. Anorg. Allg. Chem.* **226,** 391-407 (2012).

12. C. J. Pan *et al.*, An operando x-ray diffraction study of chloroaluminate anion-graphite intercalation in aluminum batteries. *Proc. Natl. Acad. Sci. U.S.A.* **115,** 5670-5675 (2018).

13. C. Yang *et al.*, Aqueous Li-ion battery enabled by halogen conversion–intercalation chemistry in graphite. *Nature* **569,** 245-250 (2019).

14. X. Zhang, Y. Tang, F. Zhang, C. S. Lee, A novel aluminum–graphite dual- ion battery. *Adv. Energy Mater.* **6,** 1502588 (2016).

15. J. Hao, X. Li, X. Song, Z. Guo, Recent progress and perspectives on dual-ion batteries. *EnergyChem* **1,** 100004 (2019).

16. S. Dühnen, R. Nölle, J. Wrogemann, M. Winter, T. Placke, Reversible anion storage in a metal-organic framework for dual-ion battery systems. *J. Electrochem. Soc.* **166,** A5474-A5482 (2019).

17. T. Placke *et al.*, Perspective on performance, cost, and technical challenges for practical dual-ion batteries. *Joule* **2,** 2528-2550 (2018).

18. M. Wang, Y. Tang, A review on the features and progress of dual- ion batteries. *Adv. Energy Mater.* **8,** 1703320 (2018).

19. A. Yamada, S. C. Chung, K. Hinokuma, Optimized $LiFePO_4$ for lithium battery cathodes. *J. Electrochem. Soc.* **148,** A224-A229 (2001).

20. W. H. Li *et al.*, Highly improved cycling stability of anion de- /intercalation in the graphite cathode for dual- ion batteries. *Adv. Mater.* **31,** 1804766 (2018).

21. Z. Li, C. Lu, Z. Xia, Y. Zhou, Z. Luo, X-ray diffraction patterns of graphite and turbostratic carbon. *Carbon* **45,** 1686-1695 (2007).

22. L. Guo *et al.*, Unlocking the energy capabilities of micron-sized $LiFePO_4$. *Nat. Commun.* **6,** 7898 (2015).

23. A. K. Padhi, K. S. Nanjundaswamy, J. B. Goodenough, Phospho- olivines as positive-electrode materials for rechargeable lithium batteries. *J. Electrochem. Soc.* **144,** 1188-1194 (1997).

24. J. Dahn, J. Seel, Energy and capacity projections for practical dual- graphite cells. *J. Electrochem. Soc.* **147,** 899-901 (2000).

25. X. Han *et al.*, An in situ interface reinforcement strategy achieving long cycle performance of dual- ion batteries. *Adv. Energy Mater.* **9,** 1804022 (2019).

26. K. Edström, T. Gustafsson, J. O. Thomas, The cathode–electrolyte interface in the Li-ion battery. *Electrochim. Acta* **50,** 397-403 (2004).

27. M. Sina *et al.*, Investigation of SEI layer formation in conversion iron fluoride cathodes by combined STEM/EELs and XPS. *J. Phys. Chem. C* **119,** 9762-9773 (2015).

28. A. Andersson *et al.*, Surface characterization of electrodes from high power lithium-ion batteries. *J. Electrochem. Soc.* **149,** A1358-A1369 (2002).

29. H. Duncan, Y. Abu-Lebdeh, I. J. Davidson, Study of the cathode–electrolyte interface of $LiMn_{1.5}Ni_{0.5}O_4$ synthesized by a sol–gel method for li-ion batteries. *J. Electrochem. Soc.* **157,** A528-A535 (2010).

30. C. Yan *et al.*, Lithium nitrate solvation chemistry in carbonate electrolyte sustains high- voltage lithium metal batteries. *Angewandte Chemie* **130,** 14251-14255 (2018).

31. X. Tong, F. Zhang, B. Ji, M. Sheng, Y. Tang, Carbon- coated porous aluminum foil anode for high- rate, long- term cycling stability, and high energy density dual- ion batteries. *Adv. Mater.* **28,** 9979-9985 (2016).

32. Y. Kadoma *et al.*, Optimization of electrochemical properties of $LiFePO_4$/C prepared by an aqueous solution method using sucrose. *Electrochim. Acta* **55,** 1034-1041 (2010).

33. M. S. Islam, D. J. Driscoll, C. A. Fisher, P. R. Slater, Atomic-scale investigation of defects, dopants, and lithium transport in the $LiFePO_4$ olivine-type battery material. *Chem. Mater.* **17,** 5085-5092 (2005).

34. L. Fan, Q. Liu, S. Chen, Z. Xu, B. Lu, Soft carbon as anode for high- performance sodium- based dual ion full battery. *Adv. Energy Mater.* **7,** 1602778 (2017).

35. A. C. Ferrari, Raman spectroscopy of graphene and graphite: disorder, electron–phonon coupling, doping and nonadiabatic effects. *Solid State Commun.* **143,** 47-57 (2007).

36. A. Manthiram, An outlook on lithium ion battery technology. *ACS central science* **3,** 1063-1069 (2017).

37. J. Seel, J. Dahn, Electrochemical intercalation of PF_6 into graphite. *J. Electrochem. Soc.* **147,** 892-898 (2000).

38. M. L. Aubrey, J. R. Long, A dual−ion battery cathode via oxidative insertion of anions in a metal–organic framework. *J. Am. Chem. Soc.* **137,** 13594-13602 (2015).

39. W. K. Pang, V. K. Peterson, A custom battery for operando neutron powder diffraction studies of electrode structure. *J. Appl. Crystallogr.* **48,** 280-290 (2015).

40. A. J. Studer, M. E. Hagen, T. J. Noakes, Wombat: The high-intensity powder diffractometer at the opal reactor. *Physica B: Condensed Matter* **385,** 1013-1015 (2006).

41. D. Richard, M. Ferrand, G. Kearley, Lamp, the large array manipulation program. *J. Neutron Research* **4,** 33-39 (1996).

42. B. H. Toby, R. B. Von Dreele, Gsas- II: The genesis of a modern open- source all purpose crystallography software package. *J. Appl. Crystallogr.* **46,** 544-549 (2013).

43. J. P. Perdew, K. Burke, M. Ernzerhof, Generalized gradient approximation made simple. *Phys. Rev. Lett.* **77,** 3865 (1996).

44. J. Hafner, Ab- initio simulations of materials using vasp: density- functional theory and beyond. *J. Comput. Chem.* **29,** 2044-2078 (2008).

45. C. Ouyang, S. Shi, Z. Wang, X. Huang, L. Chen, First-principles study of Li ion diffusion in $LiFePO_4$. *Phys. Rev. B* **69,** 104303 (2004).

46. S. Miyoshi *et al.*, Fast diffusivity of PF_6–anions in graphitic carbon for a dual-carbon rechargeable battery with superior rate property. *J. Phys. Chem. C* **120,** 22887-22894 (2016).